Electronic Supplementary Information

BiVO$_4$ Quadrangular Nanoprisms with Highly Exposed {101} Facets for Selective Photocatalytic Oxidation of Benzylamine

Min Lv,[a] Fengxia Tong,[a] Zeyan Wang,[a] Yuanyuan Liu,[a] Peng Wang,[a] Hefeng Cheng,[a] Ying Dai,[b] Zhaoke Zheng,*[a] and Baibiao Huang[a]

[a]State Key Laboratory of Crystal Materials, Shandong University, Jinan 250100, China

[b]School of Physics, Shandong University, Jinan 250100, China

*Corresponding author's email address: zkzheng@sdu.edu.cn

1 Experimental Section

1.1 Preparation of D-BiVO$_4$

D-BiVO$_4$ was synthesized by a hydrothermal method according to previously reported protocol with some modifications.[1,2] First, 4 mmol Bi(NO$_3$)$_3$·5H$_2$O and 4 mmol NH$_4$VO$_3$ were added in 30 mL of nitric acid solution (1 mol/L) under vigorous stirring until Bi(NO$_3$)$_3$ and NH$_4$VO$_3$ were completely dissolved. Then, 2.25 mL of NH$_3$·H$_2$O was added to the solution to adjust the pH under vigorous stirring. After aging for 2 h, the product was transferred to a Teflon-lined stainless steel autoclave (100 mL) and hydrothermally treated at 100 °C for 48 h. After cooling the autoclave to room temperature, a yellow powder was obtained, which was separated by centrifugation (12000 rpm, 3 min) and washed with deionized water and ethanol for more than 3 times. Finally, the products were dried at 60 °C in air for 12 h.

1.2 Photoelectrochemical tests

The photoelectrochemical performances of the catalysts were measured on an electrochemical workstation (CHI660E) with a three-electrode system at room temperature. A Pt sheet and saturated calomel electrode (SCE) were employed as the counter electrode and reference electrode, respectively. The as-prepared samples were spin-coated on clean FTO glass substrates to be used as the working electrodes. For making the working electrodes, 3 mg sample was added into 200 μL isopropanol, and then 20 μL Nafion was added into the solution. After ultrasonic for 30 min, 100 μL solution was spin-coated on the surface of FTO glass with the geometric area of 1.0×2.0 cm^2 (the illumination area was 0.5×1.0 cm^2). A 300 W Xenon lamp (CEL-HXF300) was used as the light source and all of the photoelectrochemical tests were carried out in 0.1 M potassium phosphate (KPi) at a pH value of 7.0. The linear sweep voltammetry (LSV) measurements of as-prepared samples were carried out at a scan rate of 10 mV·s^{-1}. Transient photocurrent response was measured at 1.23 V vs. RHE. Mott–Schottky plots were measured at a frequency of 1 kHz with an AC amplitude of 10 mV.

1.3 Electron spin resonance spin-trapping tests

Electron spin resonance (ESR) was employed to detect the superoxide radicals ($^{\bullet}O_2^-$) with 5,5-Dimethyl-1-pyrroline N-oxide (DMPO) as the spin-trapping agent and to detect holes (h$^+$) with 2,2,6,6-Tetramethylpiperidinooxy (TEMPO) as the spin-trapping

agent. Briefly, 3 mg samples were dispersed into 6 mL methanol containing 0.05 M DMPO and 3 mL MilliQ ultrapure water containing 2 mM TEMPO to detect $^{\bullet}O_2^{-}$ and h^+, respectively. A 300W Xenon lamp (CEL-HXF300) was used as the light source. ESR signals were recorded in the dark and after being illuminated different times using an electron spin resonance spectrometer (Bruker A300) at room temperature. The ESR signals of V_O were recorded by electron paramagnetic resonance (EPR) spectra at low temperature (100 K).

1.4 DFT calculation method

All calculations were performed based on density functional theory (DFT) using the Vienna Ab-initio Simulation Package (VASP),[3-6] with the projector augmented wave (PAW) pseudopotentials.[7] The Perdew-Burke-Ernzerhof (PBE) functional in the generalized gradient approximation (GGA) was used to describe the exchange-correlation interaction.[8] The cutoff energy for plane-wave basis was set to 400 eV. The convergence of energy and forces were set to 1×10^{-4} eV and 0.05 eV/Å, respectively. The surfaces were represented by slab models repeated periodically. For all the surface calculations a vacuum layer of more than 12 Å was used to avoid the interaction between periodic slabs. The top half of the slab and the adsorbents were allowed to relax, while the bottom half of the slab was held fixed at its optimized bulk position.

1.5 Crystal facets angles computation

The relationship between Miller indices and projection angels are suitable for monoclinic crystal system. The angle Φ between the two crystal facets $(h_1k_1l_1)$ and $(h_2k_2l_2)$ has nothing to do with Bravais lattice, but only with Miller indices themselves, which can be calculated using the following equation:

$$\cos\Phi = \frac{d_1d_2}{\sin^2\beta}\left[\frac{h_1h_2}{a^2} + \frac{k_1k_2\sin^2\beta}{b^2} + \frac{l_1l_2}{c^2} - \frac{(l_1h_2 + l_2h_1)\cos\beta}{ac}\right]$$

where d_1 and d_2 are the interplanar spacing of crystal facets $(h_1k_1l_1)$ and $(h_2k_2l_2)$ of the monoclinic $BiVO_4$ (JCPDS no. 14-0688), respectively. a, b, c and β are unit cell parameters of monoclinic $BiVO_4$. The obtained Φ between (121) and (010) crystal facets is 58.2°, between (101) and (121) crystal facets is 31.8°, and between (010) and (101) crystal facets is 90°.
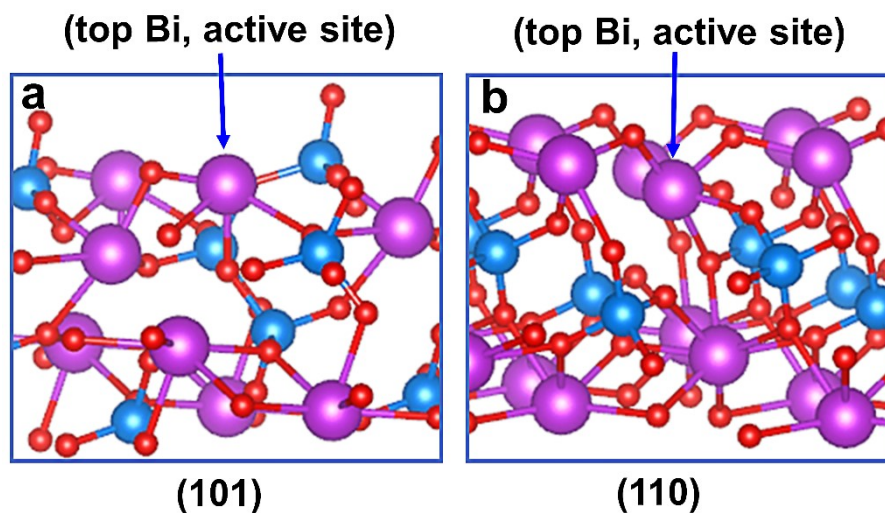
Fig. S1 (a, b) Side view of (101) and (110) facets of monoclinic BiVO₄. There are uncoordinated Bi atoms exposed on these facets, which can serve as the active sites. The red, purple and blue balls represent oxygen, bismuth and vanadium from BiVO₄, respectively.
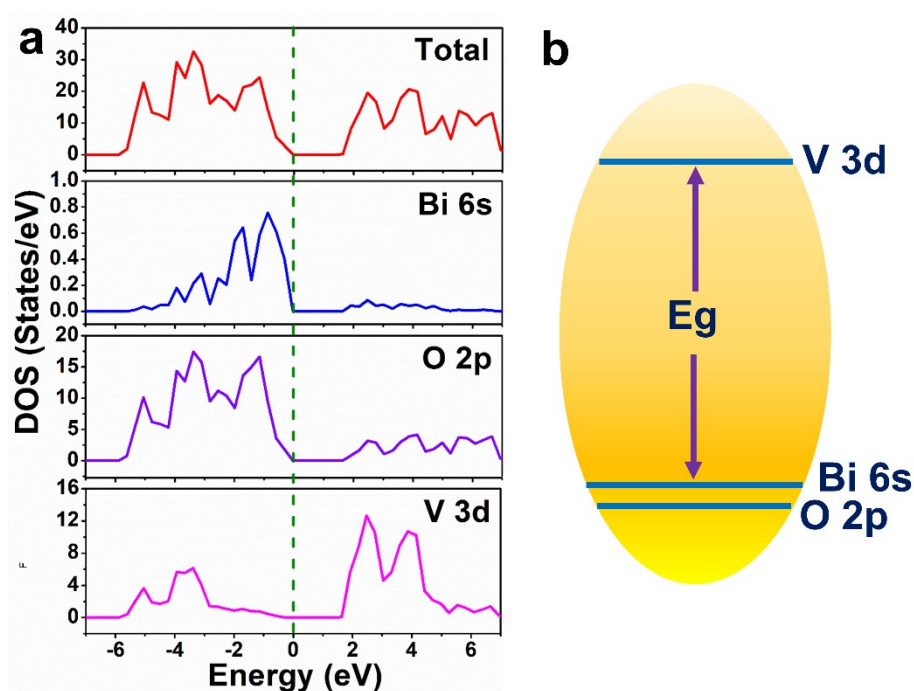
Fig. S2 (a) The TDOS and corresponding PDOSs of Bi 6s, O 2p, and V 3d for bulk monoclinic BiVO₄. The Fermi level is set to zero and represented by the green dashed line. (b) The band structure diagram of monoclinic BiVO₄.
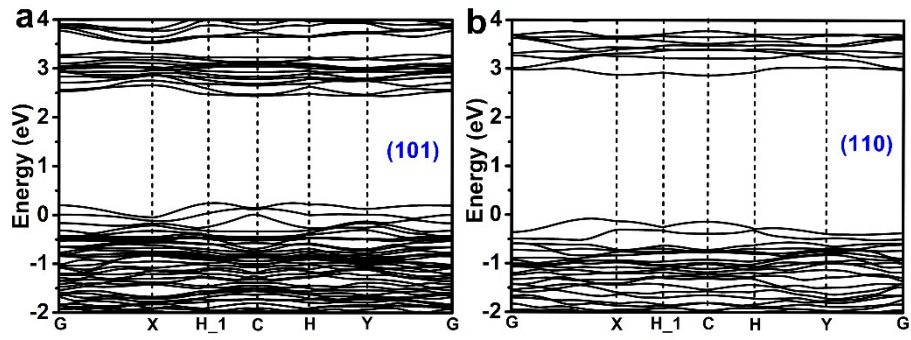
Fig. S3 The calculated energy band structures of (101) and (110) facets of monoclinic BiVO$_4$.
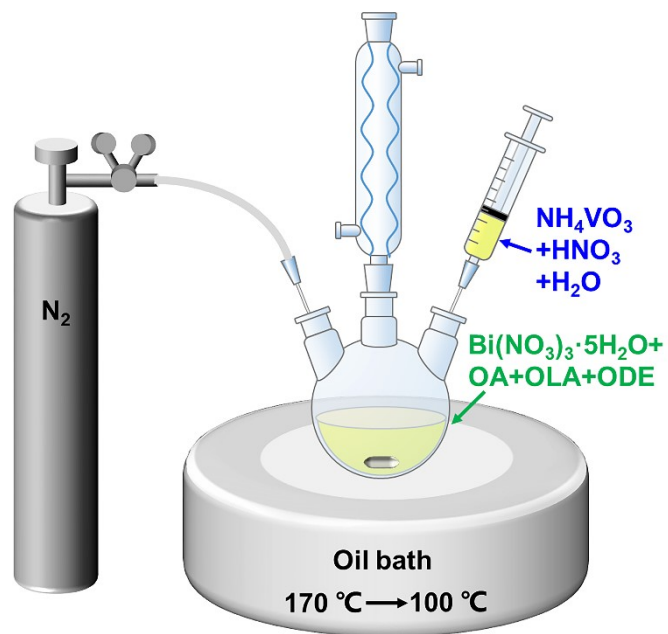
Fig. S4 Diagram of the reaction device for synthesizing Q-BiVO$_4$.
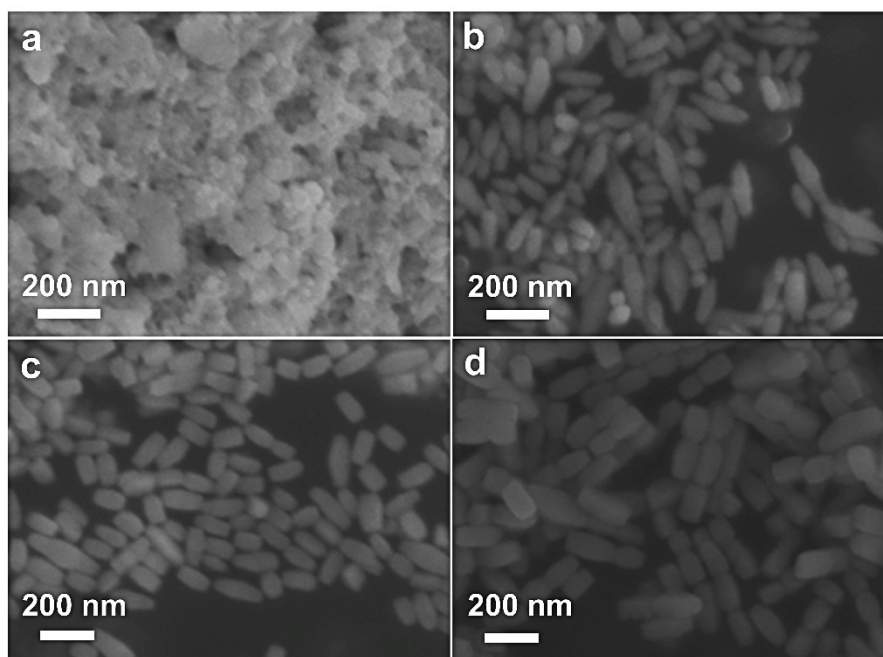
Fig. S5 Temporal evolution of the Q-BiVO$_4$ crystal growth. FESEM images showing the morphologies of the BiVO$_4$ crystals with reaction time of (a) 10 min, (b) 17 min, (c) 25 min, (d) 55 min, respectively (start timing from the beginning of adding NH$_4$VO$_3$ solution).
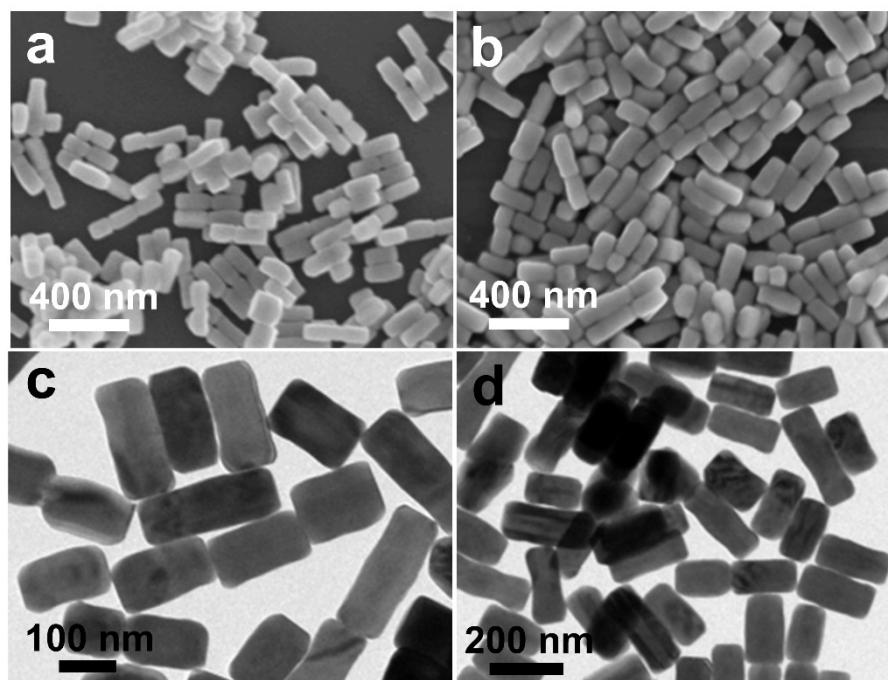
Fig. S6 (a, b) FESEM images and (c, d) TEM images of Q-BiVO$_4$.
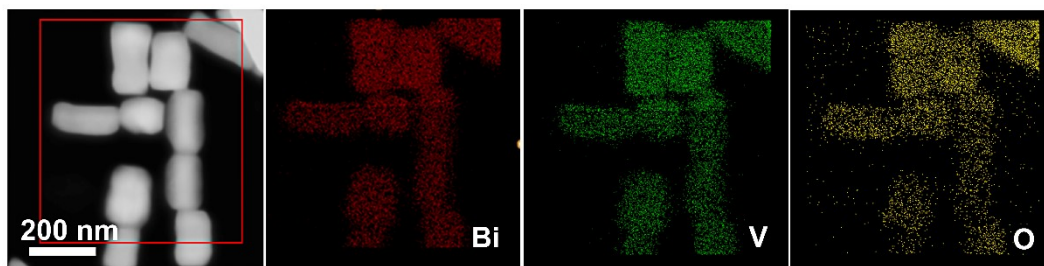
Fig. S7 Elemental mapping images of Bi, V and O of selected area for Q-BiVO$_4$.
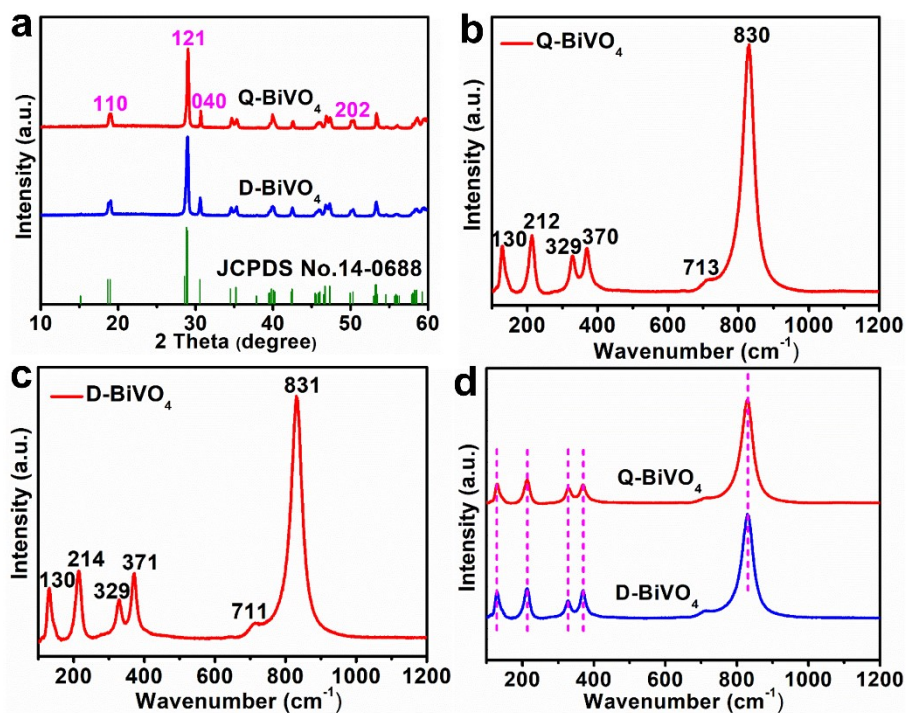
Fig. S8 (a) XRD pattern of Q-BiVO$_4$ and D-BiVO$_4$. Raman spectra of (b) Q-BiVO$_4$ and (c) D-BiVO$_4$. (d) Comparison of the Raman spectra of Q-BiVO$_4$ and D-BiVO$_4$.

Fig. S8 further confirms the monoclinic structure of Q-BiVO$_4$ and D-BiVO$_4$. As shown in Fig. S8b, the peaks around 130 and 212 cm^{-1} are the external modes (rotation/translation) of monoclinic BiVO$_4$. The asymmetric bending mode and symmetric bending mode of the VO_4^{3-} tetrahedron are at around 329 and 370 cm^{-1}, respectively. The weak shoulder at 713 cm^{-1} is assigned to the asymmetric V-O stretching mode and the peak at 830 cm^{-1} is assigned to the symmetric V-O stretching mode.
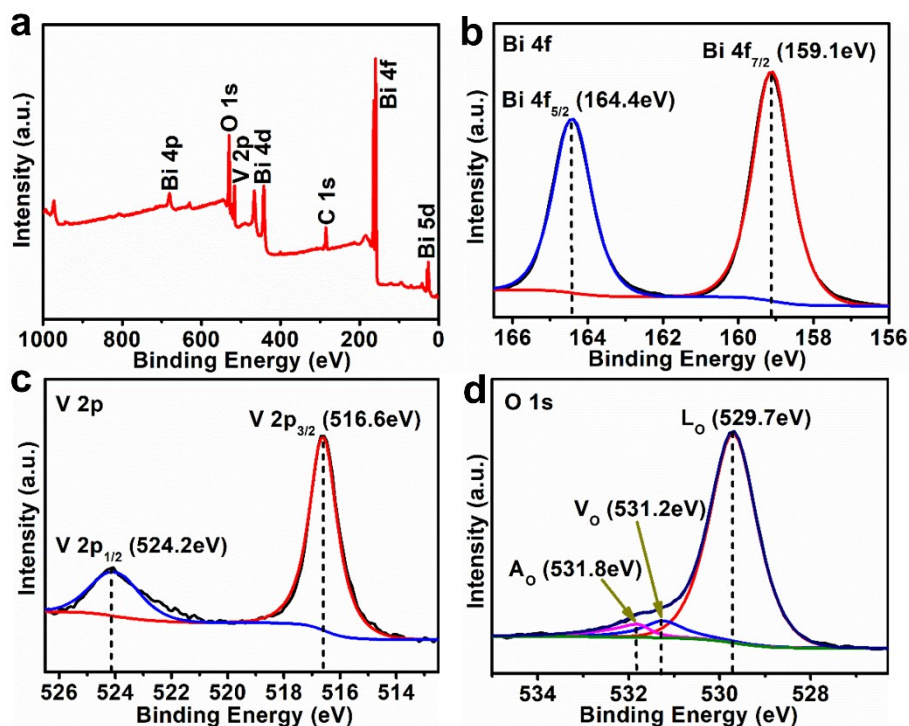
Fig. S9 (a) XPS survey spectrum of Q-BiVO$_4$. High-resolution XPS spectra of (b) Bi 4f, (c) V 2p and (d) O 1s of Q-BiVO$_4$.

The X-ray photoelectron spectroscopy (XPS) was employed to investigate the chemical states of Q-BiVO$_4$. As shown in the XPS survey spectra (Fig. S9a), Bi, V and O can be observed in Q-BiVO$_4$. High-resolution XPS spectrum of Bi 4f in Fig. S9b exhibits two peaks at 159.1 eV and 164.4 eV with a peak splitting of 5.3 eV, corresponding to the Bi 4f$_{7/2}$ and Bi 4f$_{5/2}$ orbitals of Bi^{3+} species, respectively.[9,10] The V 2p peaks (Fig. S9c) at 516.6 eV and 524.2 eV with a peak splitting of 7.6 eV, are assigned to the V 2p$_{3/2}$ and V 2p$_{1/2}$ orbitals, respectively, implying the existence of V^{5+}.[11,12] In addition, the XPS spectrum of O 1s (Fig. S9d) is deconvoluted into three different components, which can be ascribed to lattice oxygen (L$_O$) at 529.7 eV, oxygen vacancy (V$_O$) at 531.2 eV, and adsorbed oxygen (A$_O$) at 531.8 eV, respectively.[13,14] These phenomena can also be observed in D-BiVO$_4$ and nano-BiVO$_4$ (Fig. S10 and Fig. S15).
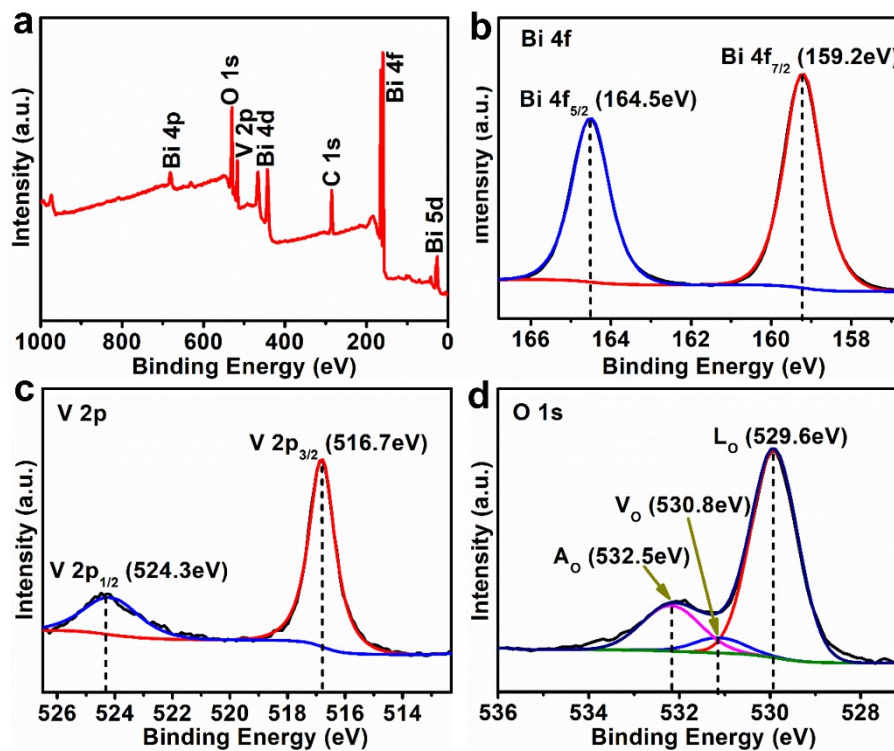
Fig. S10 (a) XPS survey spectrum of D-BiVO$_4$. High-resolution XPS spectra of (b) Bi 4f, (c) V 2p and (d) O 1s of D-BiVO$_4$.
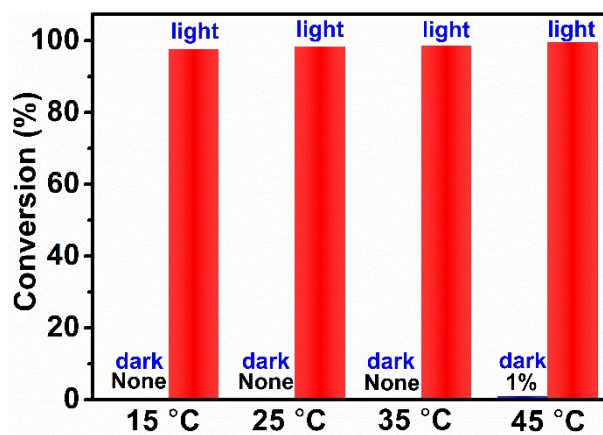
Fig. S11 The conversion efficiency over Q-BiVO$_4$ at different temperatures. Reaction conditions: 10 mg Q-BiVO$_4$, 0.1 mmol BnNH$_2$, 5 mL ACN, O$_2$ (1 atm), with or without light illumination (300 W Xenon lamp, $\lambda > 420$ nm).
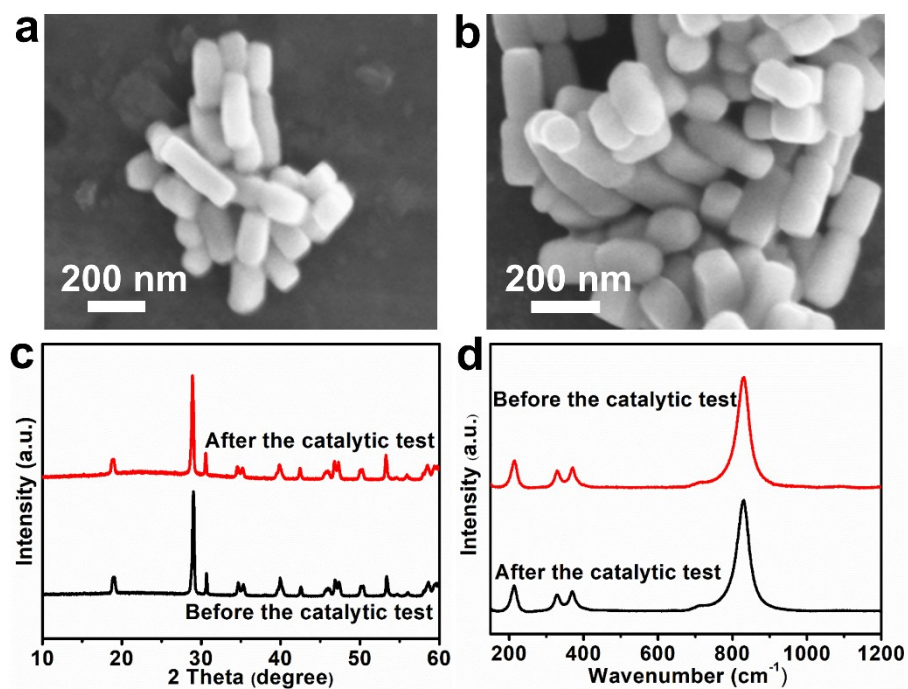
Fig. S12 (a, b) FESEM images, (c) XRD patterns and (d) Raman spectra of Q-BiVO$_4$ after cycling tests.
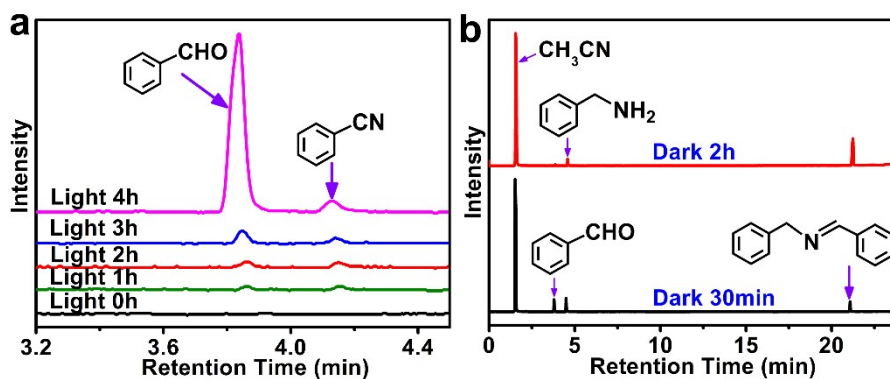
Fig. S13 (a) Partially magnified image of Fig. 4d. (b) GC-MS-FID traces of the reaction between BnNH$_2$ and benzaldehyde. Reactions conditions: 0.1 mmol BnNH$_2$, 0.1 mmol benzaldehyde, 5 ml ACN, dark for 30 min and 2 h.
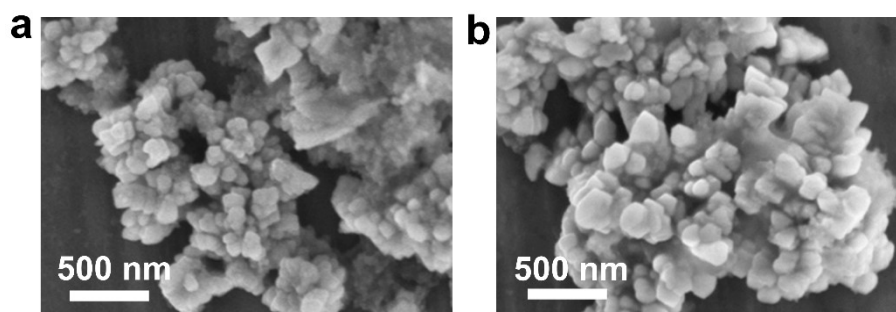
Fig. S14 (a, b) FESEM images of nano-BiVO$_4$.
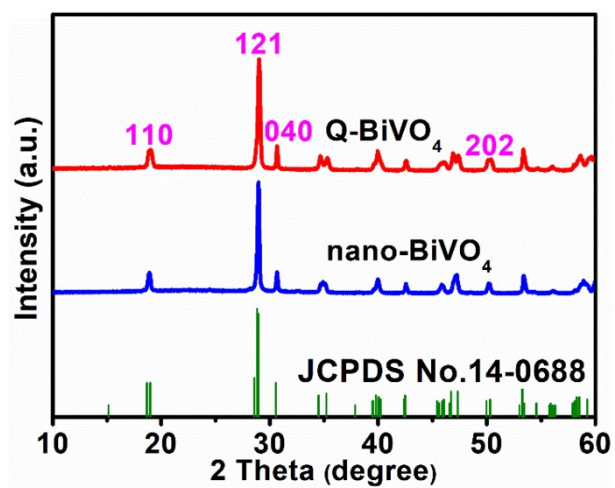
Fig. S15 XRD pattern of Q-BiVO$_4$ and nano-BiVO$_4$.
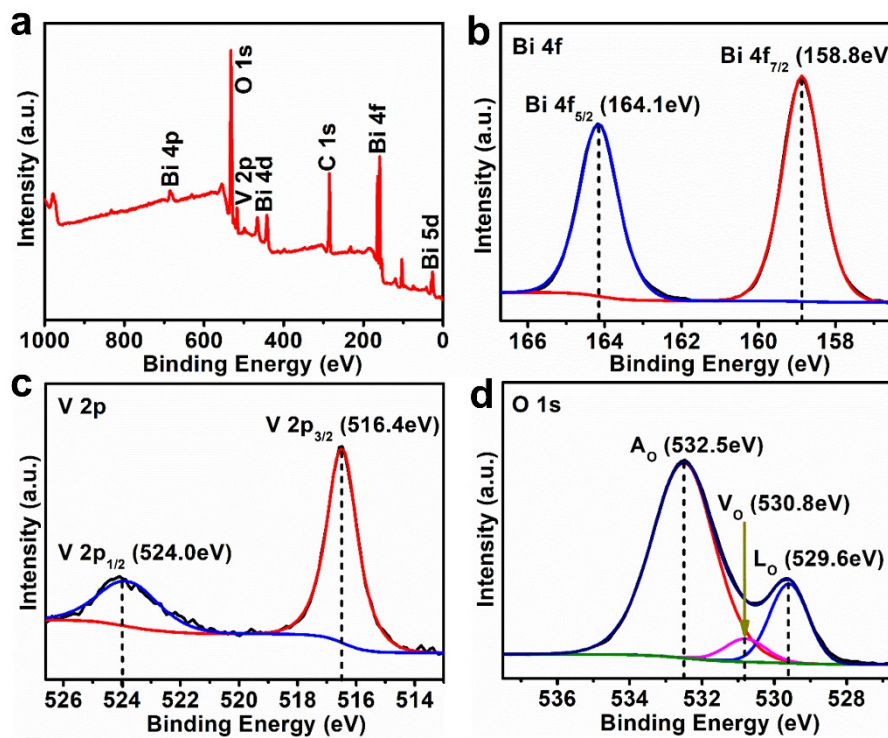
Fig. S16 (a) XPS survey spectrum of nano-BiVO$_4$. High-resolution XPS spectra of (b) Bi 4f, (c) V 2p and (d) O 1s of nano-BiVO$_4$.
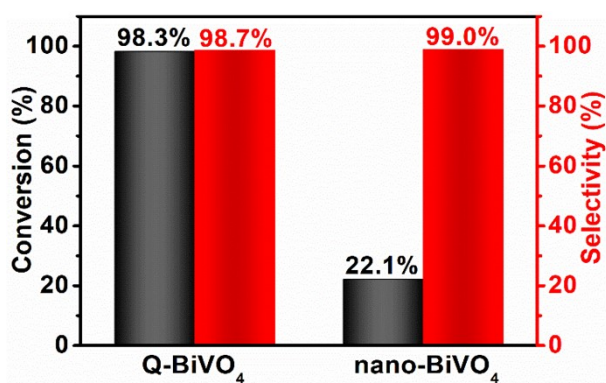
Fig. S17 The conversion efficiency and selectivity of photocatalytic BnNH$_2$ oxidation by using Q-BiVO$_4$ and nano-BiVO$_4$ as catalysts, respectively.

Table S1 Comparison of photocatalytic BnNH$_2$ oxidation with different catalysts.

Photocatalyst	Time (h)	Condition	Conversion (%)	Selectivity (%)	TOF (h^{-1})	Ref
Q-BiVO$_4$	4	λ > 420 nm	98.3	98.7	0.786	This work
nano-BiVO$_4$	4	λ > 420 nm	22.1	99.0	0.177	This work
D-BiVO$_4$	4	λ > 420 nm	48.5	95.0	0.373	This work
CuWO$_4$	180	λ$_{max}$ = 460 nm	93.0	99.0	0.040	[15]
BiVO$_4$	130	λ$_{max}$ = 460 nm	91	98	0.056	[15]
Bi$_2$M$_O$O$_6$ NPs	2	50 W LED	96.9	83.8	0.310	[16]
Bi$_2$M$_O$O$_6$ SHs	2	50 W LED	24.5	78.0	0.073	[16]
WO$_3$·H$_2$O	8	No light, 80 °C	93.0	98.0	0.285	[17]
TiO$_2$	4	λ > 420 nm	99.9	73.3	0.058	[18]
Nb$_2$O$_5$	50	λ > 300 nm	> 99	97.0	0.258	[19]
mpg-C$_3$N$_4$	3.5	λ > 420 nm, 80 °C	99	99	0.515	[20]
BiOBr-S-110	14	400-650 nm	100	100	0.022	[21]
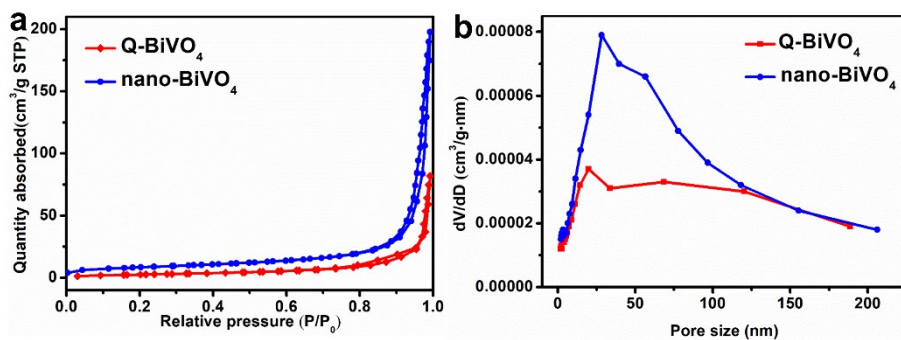
Fig. S18 (a) N_2 adsorption-desorption isotherms and (b) pore size distributions of Q-BiVO$_4$ and nano-BiVO$_4$.

Table S2 Specific BET surface areas of Q-BiVO$_4$ and nano-BiVO$_4$.

Sample	Surface area (m^2/g)
Q-BiVO$_4$	10.3220
nano-BiVO$_4$	29.4505
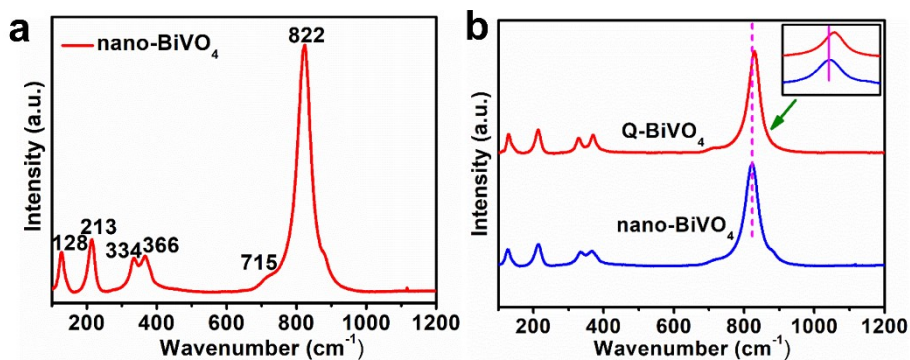
Fig. S19 (a) Raman spectra of nano-BiVO$_4$. (b) Comparison of the Raman spectra of Q-BiVO$_4$ and nano-BiVO$_4$.
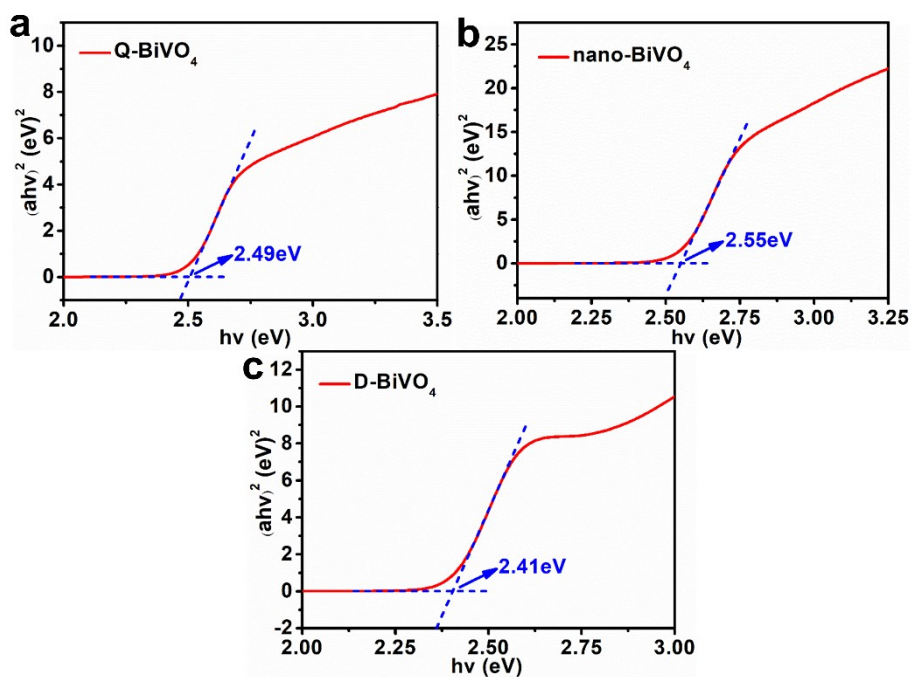
Fig. S20 Tauc plots of (a) Q-BiVO$_4$, (b) nano-BiVO$_4$, and (c) D-BiVO$_4$.
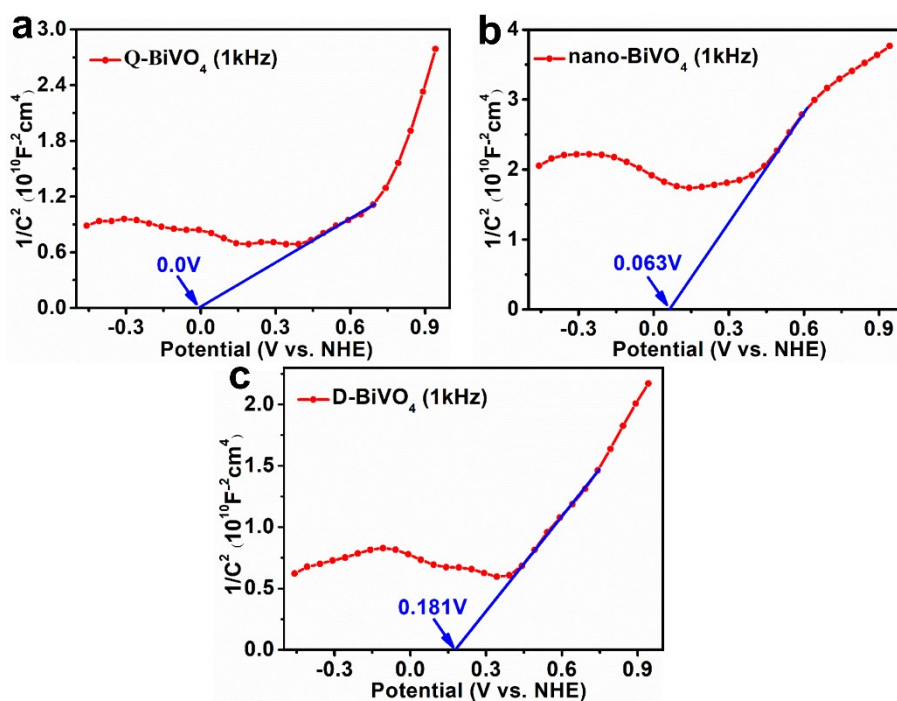
Fig. S21 Mott–Schottky curves of (a) Q-BiVO$_4$, (b) nano-BiVO$_4$ and (c) D-BiVO$_4$.
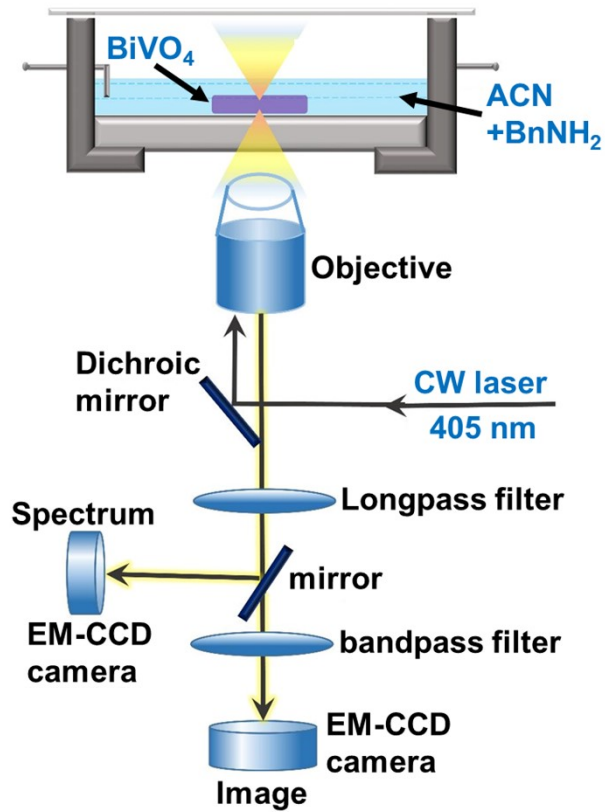
Fig. S22 Illustration of single-particle PL measurement based on confocal microscope system.
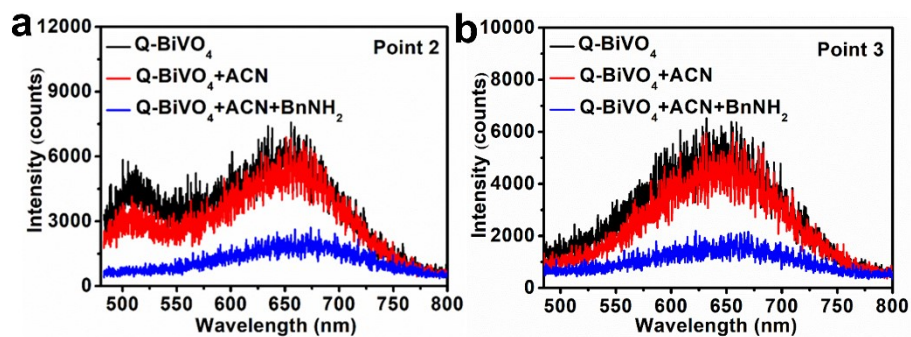
Fig. S23 (a, b) PL intensity spectra of individual Q-BiVO$_4$ as numbered "2" and "3" corresponding to the PL image in Fig. 6a, b.
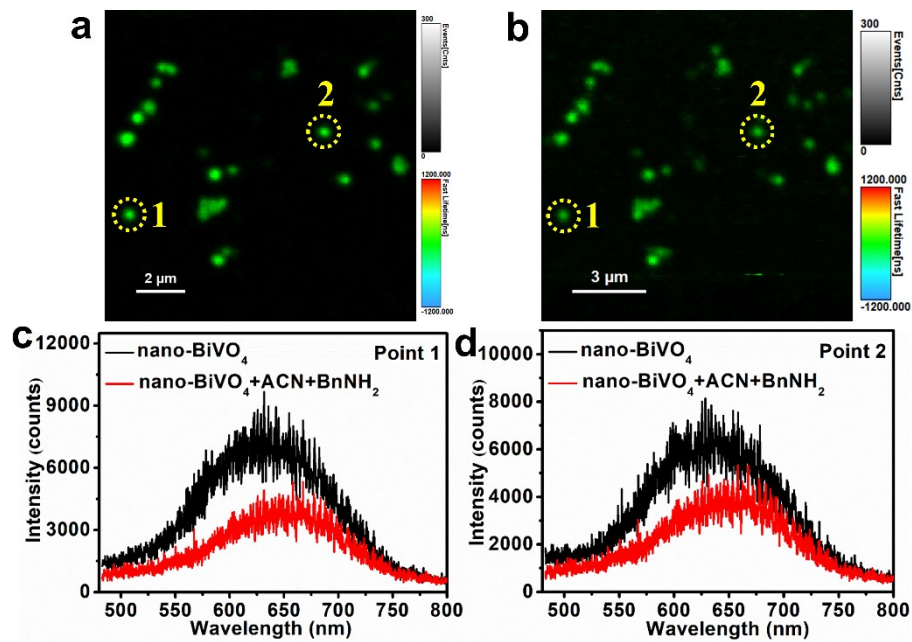
Fig. S24 PL images of nano-BiVO$_4$ dispersed on quartz cover glass (a) before adding ACN and BnNH$_2$ to the cell, and (b) after adding ACN and BnNH$_2$ to the cell. (c, d) PL intensity spectra of nano-BiVO$_4$ as numbered "1" and "2" in (a, b).
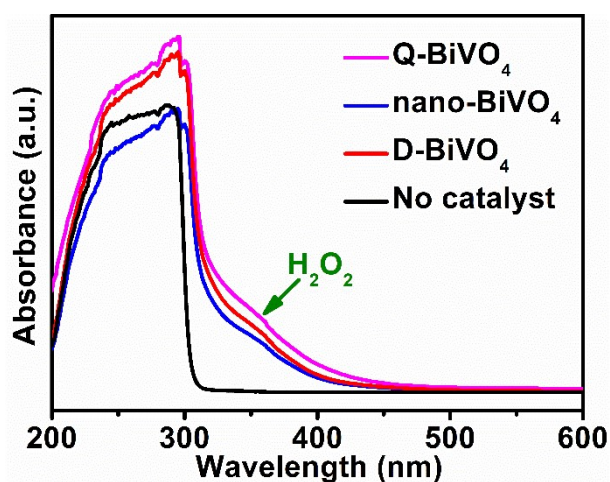
Fig. S25 UV-Vis absorption spectrum for detecting the existence of H_2O_2 by using Q-$BiVO_4$, nano-$BiVO_4$ and D-$BiVO_4$ as catalysts or without catalyst, respectively.

The formation of H_2O_2 was analyzed by iodometry. Typically, 1 mL of 0.1 mol/L potassium phthalate monobasic ($C_8H_5KO_4$) and 1mL of 0.4 mol/L potassium iodide (KI) were added to 3 ml of the detection solution, and the solution stood still for 30 min. The detection solution was obtained after photocatalytic oxidation of $BnNH_2$ by using Q-$BiVO_4$, nano-$BiVO_4$ and D-$BiVO_4$ as catalysts or without catalyst for 4 hours, respectively. H_2O_2 can react with I^- under acidic conditions to produce I_3^-, which possesses a strong absorption peak near 350 nm. As shown in Fig. S25, after light irradiation for 4 hours in the presence of catalysts, the reaction solution had an obvious absorption peak at about 350 nm, indicating that H_2O_2 was produced during the photocatalytic oxidation of $BnNH_2$ to N-BB. The absorption intensity near 350 nm for Q-$BiVO_4$ is greater than that for D-$BiVO_4$ and nano-$BiVO_4$, indicating that the amount of H_2O_2 generated by Q-$BiVO_4$ is larger than that of D-$BiVO_4$ and nano-$BiVO_4$, which is consistent with the photocatalytic $BnNH_2$ oxidation performance (Fig. 4b).

References

1. R. G. Li, F. X. Zhang, D. G. Wang, J. X. Yang, M. R. Li, J. Zhu, X. Zhou, H. X. Han and C. Li, *Nat. Commun.*, 2013, **4**, 1432.
2. T. Tachikawa, T. Ochi and Y. Kobori, *ACS Catal.*, 2016, **6**, 2250-2256.
3. G. Kresse and J. Hafner, *Phys. Rev. B*, 1993, **47**, 558-561.
4. G. Kresse and J. Hafner, *Phys. Rev. B*, 1994, **49**, 14251-14269.
5. G. Kresse and J. Furthmuller, *Comput. Mater. Sci.*, 1996, **6**, 15-50.
6. G. Kresse and J. Furthmuller, *Phys. Rev. B*, 1996, **54**, 11169-11186.

7. P. E. Blochl, *Phys. Rev. B*, 1994, **50**, 17953-17979.

8. J. P. Perdew, K. Burke and M. Ernzerhof, *Phys. Rev. Lett.*, 1996, **77**, 3865-3868.

9. X. Y. Wang, Y. S. Wang, M. C. Gao, J. N. Shen, X. P. Pu, Z. Z. Zhang, H. X. Lin and X. X. Wang, *Appl. Catal. B*, 2020, **270**, 118876.

10. B. B. Zhang, L. J. Chou and Y. P. Bi, *Appl. Catal. B*, 2020, **262**, 118267.

11. C. W. Dong, S. Y. Lu, S. Y. Yao, R. Ge, Z. D. Wang, Z. Wang, P. F. An, Y. Liu, B. Yang and H. Zhang, *ACS Catal.*, 2018, **8**, 8649-8658.

12. X. H. Cao, C. J. Xu, X. M. Liang, J. R. Ma, M. E. Yue and Y. Ding, *Appl. Catal. B*, 2020, **260**, 118136.

13. H. Wang, D. Y. Yong, S. C. Chen, S. L. Jiang, X. D. Zhang, W. Shao, Q. Zhang, W. S. Yan, B. C. Pan and Y. Xie, *J. Am. Chem. Soc.*, 2018, **140**, 1760-1766.

14. J. Wu, X. D. Li, W. Shi, P. Q. Ling, Y. F. Sun, X. C. Jiao, S. Gao, L. Liang, J. Q. Xu, W. S. Yan, C. M. Wang and Y. Xie, *Angew. Chem. Int. Ed.*, 2018, **57**, 8719-8723.

15. A. D. Proctor, S. Panuganti and B. M. Bartlett, *ChemComm*, 2018, **54**, 1101-1104.

16. W. Phasayavan, M. Japa, S. Pornsuwan, D. Tantraviwat, F. Kielar, V. B. Golovko, S. Jungsuttiwong and B. Inceesungvorn, *J. Colloid Interface Sci.*, 2021, **581**, 719-728.

17. N. Zhang, X. Li, Y. Liu, R. Long, M. Li, S. Chen, Z. Qi, C. Wang, L. Song, J. Jiang and Y. Xiong, *Small*, 2017, **13**, 1701354.

18. J. Bu, J. Fang, W. R. Leow, K. Zheng and X. Chen, *RSC Adv.*, 2015, **5**, 103895-103900.

19. S. Furukawa, Y. Ohno, T. Shishido, K. Teramura and T. Tanaka, *ACS Catal.*, 2011, **1**, 1150-1153.

20. F. Z. Su, S. C. Mathew, L. Mohlmann, M. Antonietti, X. C. Wang and S. Blechert, *Angew. Chem. Int. Ed.*, 2011, **50**, 657-660.

21. A. Han, H. Zhang, G.-K. Chuah and S. Jaenicke, *Appl. Catal. B*, 2017, **219**, 269-275.